Periodic three-dimensional assemblies of polyhedral lipid vesicles

A. Hočevar[1] and P. Ziherl[1,2]

[1]*Jožef Stefan Institute, Jamova 39, SI-1000 Ljubljana, Slovenia*
[2]*Faculty of Mathematics and Physics, University of Ljubljana, Jadranska 19, SI-1000 Ljubljana, Slovenia*

We theoretically study the structure of periodic bulk assemblies of identical lipid vesicles. In our model, each vesicle is represented as a convex polyhedron with flat faces, rounded edges, and rounded vertices. Each vesicle carries an elastic and an adhesion energy and in the limit of strong adhesion, the minimal-energy shape of cells minimizes the weighted total edge length. We calculate exactly the shape of the rounded edge and show that it can be well described by a cylindrical surface. By comparing several candidate space-filling polyhedra, we find that the oblate shapes are preferred over prolate shapes for all volume-to-surface ratios. We also study periodic assemblies of vesicles whose adhesion strength on lateral faces is different from that on basal or apical faces. The anisotropy needed to stabilize prolate shapes is determined and it is shown that, at any volume-to-surface ratio, the transition between oblate and prolate shapes is very sharp. The geometry of the model vesicle assemblies reproduces the shapes of cells in certain simple animal tissues.

PACS number(s): 87.17.Pq, 87.17.Rt, 87.18.Ed, 87.18.Hf

I. INTRODUCTION

Shapes of biological cells and their spatial arrangements are a fascinating topic that has long been pondered over [1]. Some theories propose that cell shape in certain tissues such as the mammalian epidermis is determined by the dynamics of cell division and rearrangement [2–4]. On the other hand, several types of compact cells, such as those seen in the early stages of embryonic development [5], in epithelial and epidermal tissues [6], and in *Drosophila* retina [7], have been likened to soap bubbles [1,8], thereby rationalizing their shape in terms of an equilibrium mechanical model. This analogy accounts for the round, convex shape of these cells and for their propensity to form more or less close-packed aggregates or tissues. At the same time, it identifies the surface tension as the possible effective physical force responsible for the observed morphologies and the minimal-area principle as its geometric manifestation [9]. But the scope of this analogy is limited: Minimizing the surface area at a given cell volume readily generates isometric shapes but cannot reproduce the flattened or the elongated cells seen, e.g., in squamous and columnar epithelia [10]. A different, more complex theoretical framework is needed to explain the phenomenology of cells in these tissues.

Recent studies, fueled by the growing interest in the physical origin of animal morphogenesis, have exposed two mechanisms contributing to the effective surface tension of cells. One is the cortex contractility [11–14], which tends to minimize the area of the cell membrane. On the other hand, the cell-cell adhesion between cells in a close-packed aggregate favors a membrane area as large as possible [15]. Within this framework, the behavior of cells depends on the relative magnitude of the cortex tension and the adhesion strength. At small adhesion strength the cells behave like soap bubbles and the equilibrium area of the cell is as small as possible consistent with the volume constraints. But if adhesion is strong the cell area would expand indefinitely. This unphysical behavior is regularized by introducing a restoring term which penalizes large cell area and is typically proportional to area squared [11,14]. This results in cells having a preferred

surface area. Together with either a prescribed or a preferred amount of protoplasm [14,16], this model accommodates the tendency of cells to favor a certain membrane area and cell volume as two very important morphometric parameters. It is the strong adhesion variant of this theory that is relevant for the description of tissues and other cell aggregates. But the fixed-area and fixed-volume constraints alone generate too broad a spectrum of shapes: In particular, they do not distinguish between the prolate and the oblate shapes. Clearly another mechanism is needed to determine whether cells in an assembly are elongated or flattened. The so-called differential adhesion hypothesis (DAH) [17,18] proposes that the adhesion strength is nonuniform across the cell surface, which may explain the observed cell geometry [19]. But it is possible that some other mechanical force can reproduce the same phenomenology without resorting to DAH.

Here we explore the role of the membrane bending elasticity in this context. Following the suggestions of Ref. [20] we keep the model simple and consider the limit where both cell area and volume are fixed; when combined with the bending energy, these constraints naturally correspond to lipid bilayer vesicles [21]. We theoretically study the geometry of periodic three-dimensional assemblies of identical vesicles: By considering model polyhedral vesicles, we first show that the optimal shapes should minimize the weighted total edge length. The analysis of a set of candidate shapes based on space-filling polyhedra shows that the preferred shape of cells in such an assembly is oblate. However, the extended version of the model where the adhesion strength depends on the orientation of a face does stabilize assemblies of prolate cells provided that the adhesion anisotropy is large enough.

This paper is organized as follows: In Sec. II we describe the model, Sec. III introduces the set of candidate shapes that we examine, and in Sec. IV we analyze the shape of a rounded 3-valent edge as the most common edge. Section V discusses the stability of a set of vesicle assemblies derived from polyhedral partitions of space. By comparing their respective energies, we calculate the phase diagram, which is then further elaborated in Sec. VI where we study the effects of adhesion
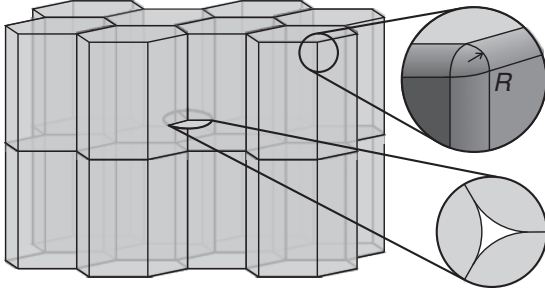
FIG. 1. An example of the model periodic three-dimensional vesicle assembly, which consists of a regular arrangement of identical rounded polyhedra. Shown here is a part of two adjacent layers of a stack of prolate regular hexagonal prisms. Each vesicle is a convex space-filling polyhedron with rounded edges and vertices (top inset). The lower inset shows the cross section of a regular 3-valent edge.

anisotropy. In Sec. VII we compare the predictions of the model with the structure of simple animal tissues and discuss possible extensions of this work. Section VIII concludes the paper.

II. MODEL

Our model periodic bulk vesicle assemblies consist of convex polyhedral shapes with flat faces and rounded edges and vertices (Fig. 1). The flat-face assumption is based on the observation of the shape of contact zones in linear assemblies where vesicles are arranged on top of one another like a stack of coins so that each vesicle has two neighbors. At small adhesion strengths, the vesicle-vesicle contact zones are curved but at large enough adhesion strengths they are planar [22,23]. Given that the three-dimensional assemblies of vesicles are expected to be stable in the large-adhesion regime, it is thus reasonable to expect that they too consist of flat-faced shapes [24]. The areas of all vesicles are identical and so are their volumes; their roundedness is described by the reduced volume

$$v = \frac{V}{4\pi R_c^3 / 3} = \frac{6\sqrt{\pi} V}{A^{3/2}}, \qquad (1)$$

where A is vesicle area, V is its volume, and

$$R_c = \sqrt{\frac{A}{4\pi}} \qquad (2)$$

is the radius of a sphere of area A. In any shape, v varies between 0 and 1; in the sphere, $v = 1$. Within the Helfrich theory [25], each vesicle is assigned an elastic energy due membrane deformations [25,26]:

$$W_b = \frac{K}{2} \oint (C_1 + C_2)^2 dA. \qquad (3)$$

Here K is the bending modulus and C_1 and C_2 are the local curvatures. Within the bilayer-couple model [26], W_b would be minimized at fixed reduced volume v and at fixed reduced lipid monolayer area difference ΔA. But in the strong-adhesion limit, the monolayer-area-difference constraint does not apply because the adhesion-induced flip-flops of lipids within the membrane relax ΔA [27] so that it is no longer considered fixed. In adhering vesicles described by the area-difference-elasticity theory [21,23,28], the magnitude of the adhesion

energy is typically much larger than that of the nonlocal bending energy and any variations from shapes with relaxed monolayer area difference are very unfavorable. Thus the nonlocal bending energy associated with the deviation of the monolayer area difference from a preferred value is subdominant for very large adhesion strengths and can be neglected. As a result, the elastic energy of the vesicles comprises the local bending energy [Eq. (3)] alone.

We model the adhesion energy by a contact potential

$$W_a = -\frac{\Gamma A_c}{2} \qquad (4)$$

proportional to the area of contact zones, as in other models [11–14]. Here Γ is the adhesion strength, A_c is the total area of the vesicle's contact zones, and each of the vesicles in contact is assigned a half of the adhesion energy associated with a pair of neighboring vesicles. The dimensionless total energy per vesicle relative to the bending energy $W_b^{\mathrm{sph}} = 8\pi K$ of a sphere is thus

$$w_{\mathrm{tot}} = w_b + w_a = \frac{1}{4} \oint (c_1 + c_2)^2 da - \frac{1}{2}\gamma a_c, \qquad (5)$$

where $c_1 = C_1 R_c, c_2 = C_2 R_c, dA = 4\pi R_c^2 da, A_c = 4\pi R_c^2 a_c$, and reduced adhesion strength

$$\gamma = \frac{\Gamma R_c^2}{2K}. \qquad (6)$$

In the limit of strong adhesion, it is reasonable to approximate the regular[1] rounded edges by parts of a cylinder (as we show in Sec. IV) and the rounded vertices by parts of a sphere of radius R. The adhering membranes experience a discontinuity of meridional curvature Δc at the point where they detach from each other [29,30]; the reduced discontinuity is given by

$$\Delta c = \sqrt{2\gamma}. \qquad (7)$$

In our model, the contact zones are flat and so the reduced curvature of the rounded edges approximated by a cylindrical surface coincides with the reduced curvature discontinuity itself: $c = \Delta c$. Thus the radius of the rounded edges reads $R = R_s / \Delta c = R_s / \sqrt{2\gamma}$. Because the curvature of all rounded parts is identical, the contact area can be written as

$$A_c = A - 4\pi R^2 - 2\pi R \sum_i \frac{d_i}{2i/(i-2)}, \qquad (8)$$

where d_i is the total length of i-valent edges of the polyhedron. The denominator in the last term takes into account that the valency of an edge determines the angle between the faces meeting at this edge. For all space-filling polyhedra that we will examine $i = 3, 4$, and 6. Thus the reduced adhesion energy of shapes with regular edges is

$$w_a = -\frac{\gamma}{2} + \frac{\gamma}{2c^2} + \frac{\gamma}{4c}\lambda. \qquad (9)$$

The first term, which is negative, represents the adhesion energy that the vesicle would have if all of its surface were in contact with the neighboring vesicles. The second and the

---

[1] In a regular 3-valent edge all faces meet at angle $120°$. In a regular 4-valent edge they meet at $90°$.

third terms are the adhesion energy deficits associated with the rounded vertices and edges, respectively. Here

$$\lambda = \frac{1}{R_c} \left(\frac{d_3}{6} + \frac{d_4}{4} + \frac{d_6}{3} \right) \qquad (10)$$

is a weighted reduced total edge length, where weights are obtained by taking into account that edges of different valence represent different lengthwise sections of a cylindrical surface. The elastic energy consists of two terms; the energy concentrated in the rounded vertices, $W_b^{\text{vert}} = 8\pi K$, and the energy of the rounded edges, $W_b^{\text{edg}} = \pi K C R_c \lambda$. The total reduced bending energy reads

$$w_b = 1 + \frac{\sqrt{2\gamma}}{8} \lambda; \qquad (11)$$

the first and the second terms correspond to vertices and edges, respectively. In the limit of strong adhesion, $\gamma \gg 1$, most of the bending energy is carried by the edges. After combining w_a and w_b, the total dimensionless energy can be written as

$$w_{\text{tot}} = \left(1 - \frac{\gamma}{2} + \frac{\gamma}{2c^2} \right) + \left(\frac{\sqrt{2\gamma}}{8} + \frac{\gamma}{4c} \right) \lambda \qquad (12)$$

and favors space-filling polyhedra that minimize the weighted total edge length λ at a given vesicle area and volume.

This formulation of the question of optimal vesicle shape in a periodic assembly somewhat resembles the Kelvin problem of partitioning space into cells of equal volume such that the area is minimal. It is also reminiscent of the so-called Melzak or waste storage problem of finding the polyhedron of unit volume (but arbitrary area) of least total edge length [31–33]. None of these problems has been solved so far. The best-known area-minimizing partition is the Weaire-Phelan structure; Kelvin's orthic tetrakaidecahedron has long been regarded as the solution [34]. For the Melzak problem, the best shape found so far is the equilateral upright triangular prism whose height is equal to the side of the base [35]. Despite the similarity, the Melzak problem differs from ours in three ways: (i) it pertains to a single polyhedron rather than to a partition of space, (ii) the polyhedron area is not fixed, and (iii) the edge length to be minimized is unweighted. Still the solutions of Kelvin and Melzak problems and their derivatives are of relevance in the present context: The former, for example, are characterized by a reduced volume larger than that achievable by prismatic shapes.

III. CANDIDATE SPACE-FILLING POLYHEDRA

We seek the optimal structure of vesicle assemblies that minimizes weighted total edge length λ among a set of 10 candidate shapes based on space-filling polyhedra[2] [36]. The simplest shapes studied are the oblate and the prolate right

---

[2]Interestingly, polyhedral shapes are expected not only in adhering vesicles but also in isolated vesicles whose membrane is composed of two types of lipids. As in our model, the energy of such shapes resides primarily in the edges, and the experimentally observed optimal shape is icosahedral [37,38]. In a theoretical analysis of the problem, the snub dodecahedron was singled out as the energetically favorable shape among the 112 convex polyhedra that were examined [39].
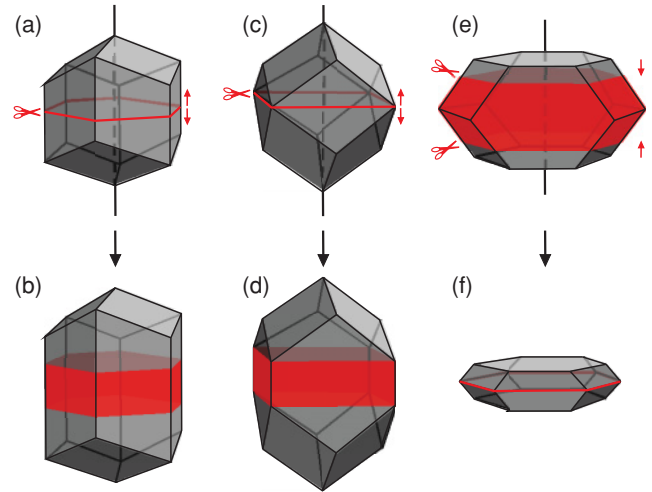

FIG. 2. (Color online) Three shapes derived from a rhombic dodecahedron. The first prolate shape shown in panel b is obtained by cutting the rhombic dodecahedron (panel a) along the mirror plane perpendicular to the three-fold axis (red line labeled by the scissor symbol) and inserting a regular hexagonal prism. This produces a prolate shape whose reduced volume depends on the height of the inserted prism. The second prolate shape (panel d) is constructed by cutting the rhombic dodecahedron in panel c along a plane perpendicular to the four-fold axis (red line labeled by the scissor symbol) and inserting a square prism. The oblate shape based on the rhombic dodecahedron is derived from the prolate shape with four-fold axis extended such that the four hexagonal lateral sides are regular (panel e). This shape is cut along two parallel planes equidistant from the mirror plane containing the four-fold axis. The central part is removed and the two caps form the oblate shape whose reduced volume is controlled by the thickness of the central part (panel f). For simplicity we refer to shapes in panels b, d, and f as 3-elongated rhombic dodecahedron, 4-elongated rhombic dodecahedron, and flattened rhombic dodecahedron, respectively.

regular triangular prisms, right square prisms, and right regular hexagonal prisms. We initially studied arbitrary triangular and quadrilateral right prisms, but it turns out that equilateral triangular prisms as well as square prisms are energetically favorable. In these shapes, all edges are regular: The angles between the faces meeting along the 3-, 4-, and 6-valent edges are $120°, 90°$, and $60°$, respectively. Thus their energy is well described by the above theory, and the same applies to the three shapes that we derive from the rhombic dodecahedron (Fig. 2). Two of them are prolate: One is obtained by cutting the rhombic dodecahedron [Fig. 2(a)] along the mirror plane perpendicular to the three-fold axis and inserting a regular hexagonal prism of a suitable height so as to generate a body

---

Although the isolated polyhedral vesicles studied in Refs. [37,38] do minimize an edge energy similar to that described by Eq. (11), the minimization is not subject to the fixed-volume constraint (because of the pores in the membrane) and the shapes need not fill the space as in a periodic assembly of adhering vesicles. Our model does include these two restrictions as well as the vesicle-vesicle adhesion energy, which is why its solutions discussed below depart from those reported in Refs. [37–39].

of desired reduced volume [Fig. 2(b)]. The other prolate shape is created by a similar transformation except that the rhombic dodecahedron is cut along the mirror plane perpendicular to the four-fold axis and a regular square prism is inserted between the caps [Fig. 2(d)]. The oblate derivative shape is obtained by taking the shape in Fig. 2(d) and cutting out some volume along the mirror plane that contains the four-fold axis [Fig. 2(f)]. These transformations preserve the geometry of all edges so that they remain regular as in the rhombic dodecahedron itself. As we show in Sec. IV, we can calculate the exact energy and shape of an arbitrary rounded edge, thus keeping the edges regular when deriving various shapes is not necessary. But the regular edge has minimal energy, which is why keeping them regular seems reasonable.

Another shape that we consider is a flattened variant of Kelvin's truncated octahedron or the orthic tetrakaidecahedron [9,40], also obtained by angle-preserving transformations producing a shape of two large parallel regular hexagonal faces and a total of six hexagonal and six rectangular lateral faces. In a regular space-filling stack of such polyhedra, the angles between adjacent faces along an edge are approximately 125.25°-125.25°-109.5°. These edges deviate from the regular 120°-120°-120° geometry and describing them as parts of a cylinder is no longer valid. They carry an energy different from that of a regular 3-valent edge and in order to evaluate the energy of a flattened body based on the truncated octahedron, we need to investigate the exact shape of rounded edges of a given geometry described by the angles between the faces.

Each space-filling polyhedron discussed here is associated with a Bravais lattice. The right square prism (shapes b and g in Fig. 6 in Sec. V) corresponds to the simple tetragonal lattice; the cube as its limiting case corresponds to the simple cubic lattice. Right regular hexagonal prisms (shapes d and j in Fig. 6) form the hexagonal lattice and so do the right regular triangular prisms (shapes a and f in Fig. 6; the unit cell consists of a pair of prisms sharing a lateral face). The rhombic dodecahedron (shape k in Fig. 6; panel a in Fig. 2) belongs to the face-centered cubic lattice and the 3-elongated rhombic dodecahedron (shape e in Fig. 6; panel b in Fig. 2) is a polyhedron based on the trigonal lattice. The 4-elongated rhombic dodecahedron (shape c in Fig. 6; panel d in Fig. 2) and the flattened rhombic dodecahedron (shape i in Fig. 6; panel f in Fig. 2) correspond to the body-centered tetragonal and the body-centered orthorhombic lattice, respectively. The trigonal lattice is represented by the flattened truncated octahedron (shape h in Fig. 6) whose limiting case—the truncated octahedron—corresponds to the body-centered cubic lattice. The only Bravais lattices not considered here are the monoclinic and the triclinic.

IV. SHAPE OF EDGES

The edges occurring in the set of candidate vesicle shapes described in Sec. III are 3-, 4-, and 6-valent. Except in the flattened truncated octahedron, all edges occurring in the trial shapes studied here are regular so the only type of irregular edge that we need to analyze in detail is the 3-valent edge, which is a closed planar contour with three cusps (Fig. 3). We break the loop into sections and first focus on one of them, for example the arc AB in Fig. 3.
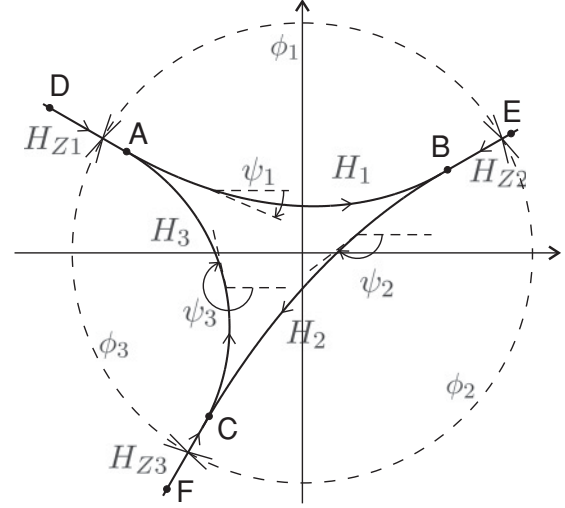

FIG. 3. Cross section of a 3-valent edge of arbitrary geometry parametrized by the angles among the contact zones ϕ_1, ϕ_2, and $\phi_3 = 2\pi - \phi_1 - \phi_2$. Sections corresponding to the contact zones (DA, EB, and FC) are straight lines and H_{Zi} denotes the corresponding Hamiltonians. The Hamiltonians of the noncontact zones (AB, BC, and CA) are denoted by H_i.

The bending energy of this section is

$$W_b = L\frac{K}{2}\int_A^B C^2 dS = l\frac{4\pi K}{2}\int_A^B c^2 ds, \qquad (13)$$

where L is the length of the edge in the direction perpendicular to the plane of cross section, dS is the arclength of the contour, and $LdS = 4\pi l R_c^2 ds$. Apart from the bending energy, the edges also carry an adhesion energy deficit [Eq. (9)]

$$W_a^{\text{def}} = L\frac{\Gamma}{2}\int_A^B dS = l\frac{4\pi R_c^2 \Gamma}{2}\int_A^B ds. \qquad (14)$$

The total dimensionless energy of arc AB per unit edge length is then

$$\widetilde{w}_{\text{AB}} = \frac{W_b}{8\pi Kl} + \frac{W_a^{\text{def}}}{8\pi Kl} = \frac{1}{4}\int_A^B c^2 ds + \frac{\gamma}{2}\int_A^B ds \qquad (15)$$

and the equilibrium shape of the contour from A to B is a stationary state of the functional $\widetilde{w}$. Since a planar continuous contour can be described by the angle between the tangent on the contour and the x axis denoted by $\psi(s)$ (see Fig. 3), we rewrite the functional as

$$\widetilde{w}_{\text{AB}} = \frac{1}{4}\int_A^B \dot{\psi}_i^2 ds + \frac{\gamma}{2}\int_A^B ds. \qquad (16)$$

After combining $\widetilde{w}_{\text{AB}}$ with $\widetilde{w}_{\text{BC}}$ and $\widetilde{w}_{\text{CA}}$, we use variational calculus to obtain a set of differential equations that need to be solved to get the stationary $\psi(s)$ of each section. The analysis also gives the boundary conditions that must be satisfied at
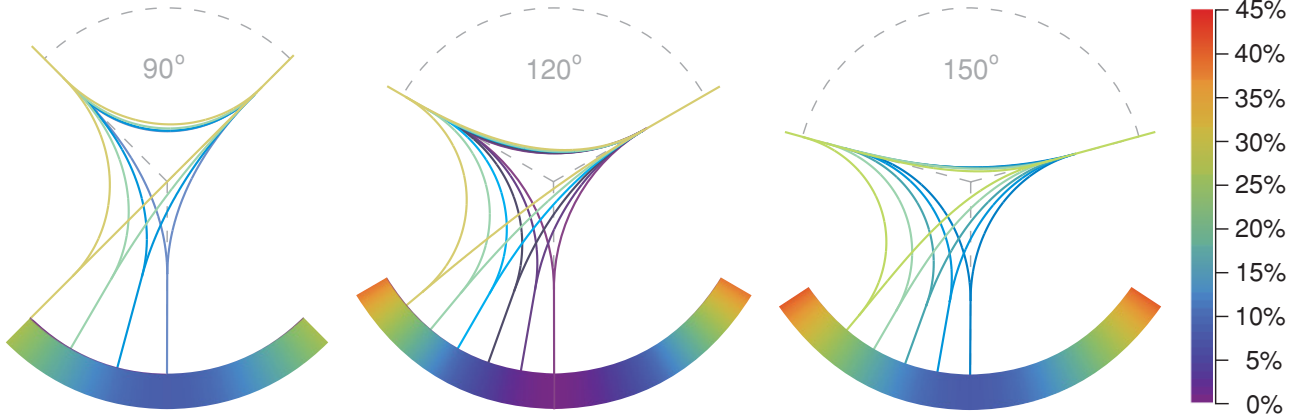
FIG. 4. (Color online) Cross- sections of the rounded edges for a few sets of (ϕ_1,ϕ_2): $\phi_1 = 90°, \phi_2 = 90°-135°$ (steps of $15°$) (left panel); $\phi_1 = 120°, \phi_2 = 70°-120°$ (steps of $10°$) (middle panel); $\phi_1 = 150°, \phi_2 = 65°-105°$ (steps of $10°$) (right panel). The cross sections are color coded to indicate the fractional increase of the edge energy per unit length relative to the regular 3-valent edge with $\phi_1 = \phi_2 = 120°$. As long as none of the angles is small, the energy increase due to a deviation from the regular configuration is moderate: the T-shaped $90°$-$90°$-$180°$ edge carries an energy 27.3% larger than the regular edge whereas the $60°$-$120°$-$180°$ edge is just short of 40% above the regular edge. The magnitude of the reduced adhesion strength γ affects only the length scale of the curved noncontact arcs of edge cross section but not their shape. Thus the cross sections shown here are the same in all edges of a given geometry specified by ϕ_1 and ϕ_2: The shape of an edge is independent of γ and so is the fractional increase of energy.

the cusps (points A, B, and C). These conditions read (see the Appendix)

$$\dot{\psi}_{1A}^2 + \dot{\psi}_{3A}^2 = 4\gamma,$$
$$\dot{\psi}_{2B}^2 + \dot{\psi}_{1B}^2 = 4\gamma, \qquad (17)$$
$$\dot{\psi}_{2C}^2 + \dot{\psi}_{3C}^2 = 4\gamma,$$

where $\dot{\psi}_{1A}$ and $\dot{\psi}_{3A}$ are the dimensionless curvatures at point A of contours 1 and 3, respectively, etc. A similar condition was obtained in a study of rouleau-like vesicle assemblies [22] where the discontinuity in the membrane curvature at the point where two membranes detach from one another equals $\sqrt{2\gamma}$. Thus Eq. (17) can be regarded as a generalization of the previously derived boundary conditions [22,30] for the case of unequal discontinuities, provided the contact zones are flat.

We solve the differential equations for a given set of angles ϕ_1, ϕ_2, and $\phi_3 = 2\pi - \phi_1 - \phi_2$ numerically and obtain the energy and the shapes of the contours. The results show that the optimal configuration of a 3-valent edge is indeed the regular geometry where $\phi_1 = \phi_2 = \phi_3 = 120°$ and the contours are parts of a circle. Our assumption that the regular rounded edges in periodic bulk lipid vesicle assemblies are cylindrical is thus justified *a posteriori*. Figure 4 shows the contours of a few irregular edge geometries along with the corresponding energies measured relative to the regular 3-valent edge. Although the energy cost for an irregular edge configuration increases rather slowly as the angles deviate from the optimal $120°$-$120°$-$120°$ geometry, it becomes significant in the limiting configurations such as the T-junction (left panel in Fig. 4), which has an energy density that exceeds the energy density of a regular edge by 27.3%.

Figure 5 shows the edge energy landscape near the minimum at $\phi_1 = \phi_2 = 120°$, which emphasizes that the energy cost of an irregular edge increases rather slowly as ϕ_1 and ϕ_2 depart from $120°$. For example, a 3-valent edge in the Kelvin space-filling polyhedron, where faces meet at

angles $125.26°$-$125.26°$-$109.47°$, carries an energy density that exceeds that of a regular angle configuration by a mere 1.03%. Along the line $\phi_1 = \phi_2$ (dashed line in Fig. 5) the relative energy landscape is well approximated by the parabolic profile given by $0.036(\phi_1 - 120)^2$.

V. COMPARISON OF SPACE-FILLING POLYHEDRA

After having dissected the structure of the edges, we can compare the energies of the model vesicle shapes presented in Sec. III. Figure 6 shows the reduced edge length of all candidate shapes as a function of reduced volume v; the main message of the comparison is that the oblate shapes are preferred over the prolate ones. For example, in a prolate square prism of $v = 0.3$, the weighted reduced edge length is $\lambda = 8.26$, whereas in an oblate square prism of
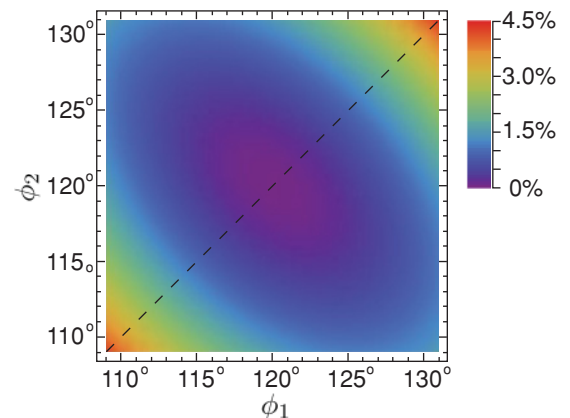

FIG. 5. (Color online) Close-up of the energy landscape of a 3-valent edge in the vicinity of the regular configuration with $\phi_1 = \phi_2 = 120°$. For deviations smaller than $10°$, the fractional increase of the edge energy does not exceed 4.5%.
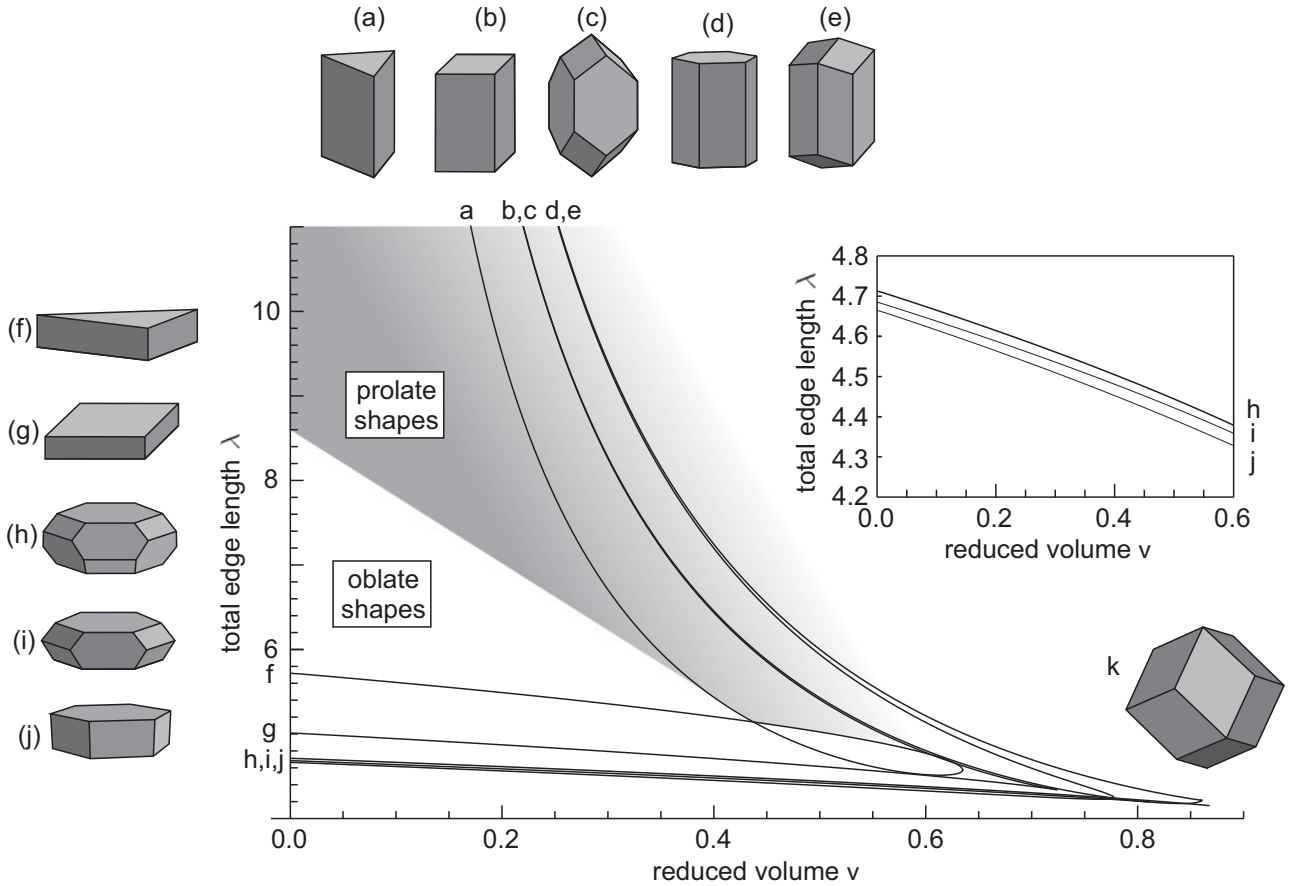
FIG. 6. Reduced edge length λ as a function of reduced volume v for the different polyhedra examined: elongated equilateral triangular prism (a), elongated square prism (b), 4-elongated rhombic dodecahedron (c), elongated hexagonal prism (d), 3-elongated rhombic dodecahedron (e), flattened equilateral triangular prism (f), flattened square prism (g), flattened truncated octahedron (h), flattened rhombic dodecahedron (i), flattened hexagonal prism (j), and rhombic dodecahedron (k). Shape k is represented in the graph as a point at $v = \sqrt{\pi}/2^{1/4}\sqrt{3} \simeq 0.861$ and $\lambda = 4.215$. The polyhedron with maximal reduced volume v is the truncated octahedron with $v = 0.868$. The oblate shapes are energetically favorable across the whole range of v; the hexagonal prism is the overall optimal shape. The inset shows the reduced edge length of the three shapes with almost identical energy: flattened hexagonal prism (j), flattened rhombic dodecahedron (i), and flattened truncated octahedron (h). Note that the energies of shapes b and d are only slightly lower than those of shapes c and e, respectively.

identical v, $\lambda = 4.79$. Among the polyhedra that we examined, the hexagonal prism is the optimal shape across a broad range of reduced volumes v. It is closely followed by a flattened rhombic dodecahedron and a flattened Kelvin cell, where the energy cost due to irregular edge geometry was taken into account. These three shapes share a pair of large parallel hexagonal faces but their lateral sides are not the same. In a similar fashion, the weighted reduced edge lengths of an elongated square prism and the 4-elongated rhombic dodecahedron are almost identical (curves b and c in Fig. 6). These two shapes are both characterized by a four-fold symmetry but their caps are different. The same holds for the caps of the elongated hexagonal prism and the 3-elongated rhombic dodecahedron; the main axis of these two shapes is not the same but their total edge lengths are very close (curves d and e in Fig. 6). Based on these observations, we conclude that the polyhedra can be classified according to the overall symmetry imposed by the shape of their largest faces (in oblate bodies) or the number of lateral sides (in prolate bodies) and that the energies of polyhedra belonging to the same class are generally very similar.

In Fig. 6, we plot the reduced edge length of the candidate shapes against their reduced volume in the limit of $\gamma \to \infty$ where the area of the noncontact part of the vesicle membrane vanishes (so that the edges and vertices are sharp). This is consistent with the formulation of the minimal-edge-length problem as proposed in Sec. II. However, at finite adhesion strength γ edge length λ is slightly smaller than that of the limiting shape at $\gamma \to \infty$ due to rounded edges and vertices. At $\gamma = 100$ this effect does not exceed a few percent and of course decreases with increasing γ. It is of similar magnitude for all candidate shapes and does not alter the above qualitative conclusions.

VI. ANISOTROPIC ADHESION

The phase diagram of the model discussed above is rather plain: For reduced volumes smaller than 0.777, the stable shape is the flattened hexagonal prism, whereas for $0.777 < v < 0.811$ it is the flattened rhombic dodecahedron (shape i in Fig. 6), and for $0.811 < v < 0.845$ it is the 4-elongated rhombic dodecahedron (shape c in Fig. 6) and for v beyond

0.845 it is the flattened truncated octahedron (shape h in Fig. 6; note that in this regime, the degree of flattening is negligible). It seems quite natural to ask under what conditions would the prolate shapes be preferred to the oblate shapes. Given the clear distinction between the lateral and basal or apical faces seen in all candidate polyhedra, the simplest extension of the model that may generate stable prolate shapes is the hypothesis of anisotropic adhesion, where the adhesion strengths on the lateral and the basal or apical faces are not identical. A suitable way of parametrizing the discrepancy of the two adhesion strengths is by the adhesion anisotropy

$$\alpha = \frac{\gamma_L}{\gamma_{BA}}, \tag{18}$$

where γ_L and γ_{BA} are the adhesion strengths on the lateral and the basal or apical sides, respectively. While anisotropic adhesion may be difficult to induce in pure lipid vesicles, which are a passive system, it is characteristic of many animal cells where it is caused by rearrangements of proteins that regulate adhesion [41].

Since the polyhedra can be classified in terms of their overall symmetry, we now only examine hexagonal, square, and triangular prisms, which simplifies the analysis. In the model explored here, the cross section of a rounded edge is constructed using elliptical rather than circular arcs to allow for the dissimilar adhesion strengths on the contact zones radiating from the edge. Rounded vertices are described by parts of a spheroid.

As in the isotropic variant of the model, each vesicle is assigned an elastic and an adhesion energy. But the total energy functional is much more complex because the rounded edges consist of elliptical arcs and because minimization of the total reduced edge length λ competes with maximization of areas of faces with large adhesion strength. For each value of adhesion anisotropy α, we construct an energy diagram analogous to Fig. 6 to determine the stable shapes across the whole range of reduced volumes, and we plot the phase diagram of stable shapes as a function of adhesion anisotropy α and vesicle reduced volume v (Fig. 7). Hexagonal prisms are optimal in the whole region where oblate shapes are preferred, whereas triangular, square, and hexagonal prolate prisms take turns in the prolate region of the diagram. It takes a fairly large adhesion
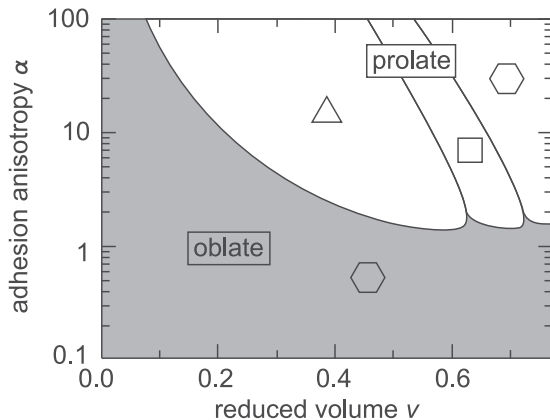
anisotropy for the prolate shapes to win over oblate ones at reduced volumes $v < 0.2$, but such vesicles are extremely deflated; the more relevant regime is at v values beyond 0.3 or 0.4. For $v > 0.5$, the boundary between prolate and oblate shapes is roughly independent of reduced volume v and is at around $\alpha = 1.5$.

To quantitatively characterize the oblate and prolate shapes, we introduce the aspect ratio as

$$\xi = \frac{b}{d}, \tag{19}$$

where b is the vesicle height and d is the diameter of the circle whose area is identical to the area of the base of the prism. In Fig. 8, we plot ξ versus adhesion anisotropy α at fixed reduced volumes $v = 0.25, 0.45, 0.65$, and 0.777. The aspect ratio is a steplike function of adhesion anisotropy, the steps corresponding to the transitions between the different shapes. The largest discontinuity occurs at the oblate-prolate transition and its magnitude decreases with v. Given the steplike shape of the curves in Fig. 8, it seems reasonable to characterize them by the value of ξ below and above the main oblate-prolate transition (ξ_o and ξ_p, respectively). In Fig. 8(b) we plot ξ_o and ξ_p as a function of the reduced volume. This diagram contains the main information on the aspect ratios of vesicles in the low and high adhesion anisotropy
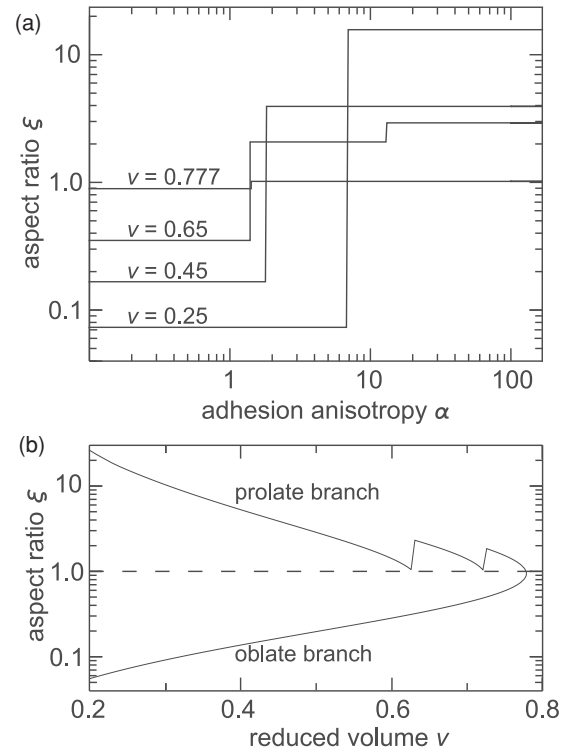

FIG. 7. Phase diagram of prismatic shapes as a function of adhesion anisotropy α and reduced volume v. Oblate hexagonal prisms are optimal at small values of adhesion anisotropy (shaded region), whereas prolate prisms are stable at large α.

FIG. 8. (a) The aspect ratio ξ of stable prismatic shapes of $v = 0.25, 0.45, 0.65$, and 0.777 as a function of adhesion anisotropy α showing that the magnitude of discontinuity in ξ decreases with reduced volume. (b) The aspect ratio of the oblate ξ_o and the prolate ξ_p vesicles stable in the small and large adhesion anisotropy regimes, respectively. As v is increased, the difference in ξ between the two branches decreases; shapes at large v are fairly isometric, neither flattened nor elongated.

regime at a given v. For example, at $v = 0.5$ the prolate shape with aspect ratio $\xi_p = 2.9$ is stable at large α and the oblate shape with $\xi_o = 0.2$ is optimal at small α. The difference between ξ_p and ξ_o decreases as reduced volume v is increased, both limiting to 1 at $v = 0.778$, which is the largest reduced volume occupied by a right regular hexagonal prism. However, the aspect ratio of the prolate shape ξ_p also approaches 1 at $v = 0.63$ and $v = 0.72$, which corresponds to the largest reduced volume occupied by a right square prism and right regular triangular prism, respectively.

The geometry of the prismatic space-filling shapes is controlled by the vesicle reduced volume and not by the energy to be minimized. At any given reduced volume, there exists one oblate and one prolate prismatic shape of a certain symmetry and their aspect ratios depend exclusively on v. But their relative stability is determined by the various types of mechanical energy. The above results show that in our model, anisotropic adhesion is needed to stabilize the prolate shapes. This would also happen in a model stripped of the bending energy provided that the adhesion strength on lateral faces is sufficiently larger than that on basal or apical faces. A simple calculation shows that in a membrane of no bending rigidity, oblate hexagonal prismatic shapes are stable at $\alpha < 1$ whereas prolate hexagonal prismatic shapes are stable at $\alpha > 1$ irrespective of reduced volume v. By comparing the threshold with the phase diagram shown in Fig. 7, we find that the effect of bending rigidity of the lipid membrane is to extend the region of stability of the oblate shapes. Specifically, in vesicles of reduced volume larger than about 0.5, the threshold is increased from $\alpha = 1$ to $\alpha \approx 1.5$ roughly independently of reduced volume.

VII. DISCUSSION

The geometry of animal tissues relies on a range of intra- and extracellular structures, interactions, and processes much more complex that those discussed here, and we cannot expect that a model as simple as ours could be relevant for their description. But there exist some tissues which consist of convex polyhedral cells of reasonably regular polyhedral shape; this typically holds for tissues with a small amount of extracellular matrix. Notwithstanding the above reservations, we find it instructive to compare our results with selected animal tissues discussed below.

A. Mammalian epidermis

The most direct and the most ordered example of a bulk-like tissue consisting of flattened cells that we are aware of is the top part of the mammalian epidermis, which consists of polyhedral keratinized cells stacked in interdigitated columns. Figure 2 in Ref. [40] exposes the cells in mouse ear epidermis, which are very similar to the flattened truncated octahedron discussed in Sec. V. Their two largest faces are hexagonal whereas the shape of the lateral faces is somewhat less regular; yet the cell is clearly not prismatic. From Fig. 2 in Ref. [40], one can estimate the reduced volume v of cells, which is around $v \approx 0.6 \pm 0.1$, and the aspect ratio $\xi \approx 0.25 \pm 0.05$. These values are consistent with the shapes predicted by either the isotropic-adhesion or the anisotropic-adhesion variant of our
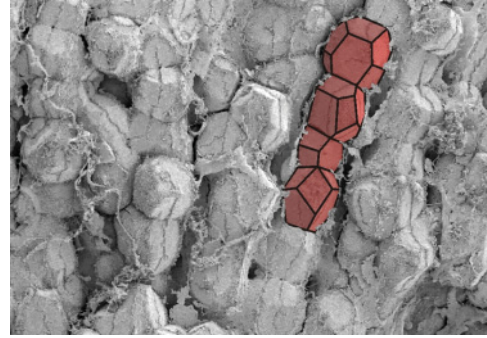

FIG. 9. (Color online) Scanning electron microscope (SEM) image of hepatocytes in mammalian liver: The roughly isometric cells are polyhedral but not identical in shape. The dilations between some cells are the bile canaliculi. Despite the irregularity of the polyhedral shape of cells, their columnar stacking demonstrates a certain degree of cell positional order. A column of cells is outlined and colored (shaded) to emphasize the polyhedral shapes and should merely serve as a guide to the eye. Image courtesy of Dr. R. Wagner, University of Delaware.

model; in the latter case, the adhesion anisotropy α should be smaller than 1.37.

B. Hepatocytes

Hepatocytes in liver are another example of an assembly of polyhedral cells. These cells are compact, devoid of any protrusions, and roughly isometric. In Fig. 9, the predominantly flat faces and the convex polyhedral shapes of hepatocytes are clearly seen. However, hepatocytes are separated by the dilations called bile canaliculi so that they do not constitute a truly space-filling packing. In addition, the shape of hepatocytes varies from cell to cell so that while the columns of cells can be easily identified, the overall regularity is not as pronounced as in epidermis. The diversity of observed cell shapes, whose reduced volume is clearly large because they are isometric, is consistent with the small energy differences between the various space-filling polyhedra predicted by our model at large v. Figure 6 shows that, for $v > 0.7$, the energies of the trial shapes differ by no more than a few percent. As a result, some variation in shape as well as the associated positional disorder is expected in any experimental realization of our model.

C. Epithelia

The three main classes of epithelial tissues include squamous, cuboidal, and columnar epithelia [10]. The first two types consist of oblate and isometric cells, respectively, which are generally similar to those discussed in Secs. VII A and VII B. A columnar epithelium, on the other hand, is made of prolate cells. The simple columnar epithelium is a single sheet of closely packed prolate cells lying on the basement membrane and facing lumen. Such an epithelium can be regarded as a layer of a limiting case of a bulk stack with infinitely large adhesion anisotropy so that the adhesion between the adjacent layers is vanishingly small compared to the intralayer adhesions.

An example of a simple columnar epithelium is shown in Fig. 1 of Ref. [42]. From this image one can estimate the

reduced volume of cells, which is 0.6 ± 0.1, and the cell aspect ratio $\xi \approx 4.5 \pm 1.0$. Such a large aspect ratio is consistent with a very large adhesion anisotropy α [19]. For $v \approx 0.6$, the anisotropic-adhesion variant of our model predicts a cell aspect ratio of $\xi \simeq 3.8$ provided that $\alpha > 30$. It remains to be verified whether such an adhesion anisotropy is reasonable.

At this junction, we note that it is not easy to imagine that a large adhesion anisotropy could exist in truly bulk tissues unless cells themselves were anisotropic; in this case, anisotropic adhesion would be the result rather than the cause of a specific cell shape. But if the most common bulk aggregates are characterized by isotropic adhesion, they should consist of either flattened or isometric cells depending on the reduced volume. This conclusion seems to agree with the fact that the stratified, multilayer epithelia typically consist of squamous or cuboidal cells whereas the stratified columnar epithelia are rare.

VIII. CONCLUSIONS

Using the Helfrich membrane bending energy and the contact-potential model of vesicle-vesicle adhesion, we have theoretically explored the structure of periodic three-dimensional assemblies of identical lipid vesicles. We have shown that at a given vesicle area and volume, the optimal shape of members of such an assembly minimizes the weighted total edge length. Across a broad range of reduced volumes, the equilibrium vesicle shape in assemblies held together by isotropic adhesion is an oblate hexagonal prism. We have extended the model by introducing adhesion anisotropy which distinguishes between the lateral and the apical or basal faces of vesicles, and we have have determined the threshold value of the anisotropy needed to stabilize the prolate shapes.

With these techniques for preparation of sizable quantities of monodisperse vesicles [43], our predictions can be readily verified experimentally. We also find that the bending elasticity of the vesicle membrane enhances the stability of flattened shapes compared to the model based on cortical tension and intercellular adhesion alone. In our model, the energy of the assembly is directly associated with the edges of the polyhedral vesicle shapes. This framework may provide a tractable way of computing the elastic moduli of an assembly, thereby constituting a coarse-grained description of the mechanics of simple tissues such as epithelia [44].

The set of polyhedra studied here is limited to single-cell partitions of space. Given that all low-energy shapes share the same overall features, it seems unlikely that the more complex space-filling structures consisting of two or more dissimilar polyhedra per unit cell would be considerably better than those discussed above. Nonetheless, we note that, at very large reduced volumes, structures based on the A15 lattice [34] or its variants [45] should be considered simply because at $v > 0.868$ there exists no single-cell polyhedral partition of space.

ACKNOWLEDGMENTS

APPENDIX

To determine the shape and the energy of a 3-valent rounded edge of arbitrary geometry, we break the loop that describes the edge into sections (Fig. 3). The total dimensionless energy per unit length of arc AB is given by Eq. (15) and a similar functional corresponds to each section of the loop. If we describe the arc by function $y(x)$,

$$\widetilde{w} = \int_A^B \mathcal{L}\,dx, \tag{A1}$$

where $\mathcal{L}(x, y, y')$ is the Lagrange function

$$\mathcal{L} = \frac{1}{4}\frac{y''^2}{(1 + y'^2)^{5/2}} + \frac{\gamma}{2}\sqrt{1 + y'^2}. \tag{A2}$$

The corresponding Euler-Lagrange equation yields a fourth-order differential equation,

$$\frac{-5y''^3 - 20y'''y''y'}{(1 + y'^2)^{7/2}} + \frac{35y''^3 y'^2}{(1 + y'^2)^{9/2}} + \frac{2y^{(4)}}{(1 + y'^2)^{5/2}}$$
$$+ \frac{2\gamma y'^2 y''}{(1 + y'^2)^{3/2}} - \frac{2\gamma y''}{(1 + y'^2)^{1/2}} = 0, \tag{A3}$$

which is solved along with the boundary conditions in points $A(x_A, y_A)$ and $B(x_B, y_B)$,

$$y(A) = k_A x_A, \quad y'(A) = k_A, \tag{A4}$$
$$y(B) = k_B x_B, \quad y'(B) = k_B, \tag{A5}$$

that come from the fact that points A and B lie on the two contact zones which are lines with coefficients k_A and k_B that are determined by ϕ_1. For a given set of angles ϕ_1, ϕ_2, $\phi_3 = 2\pi - \phi_1 - \phi_2$, and points A, B, C, the contours of all three sections are obtained by solving Eq. (A3). But coordinates of points A, B, and C are yet to be determined. The condition that yields A, B, and C that minimize the total energy is obtained using variational calculus.

A two-dimensional contour can also be described by $\psi(s)$, the angle between the tangent on the contour and the x axis. In this case, the reduced energy per unit length for section i is

$$\widetilde{w} = \frac{1}{4}\int_A^B \dot{\psi}_i^2\,ds + \frac{\gamma}{2}\int_A^B ds, \tag{A6}$$

and thus the Lagrange function for this section is

$$\mathcal{L}_i = \frac{1}{4}\dot{\psi}_i^2 + \frac{\gamma}{2} \tag{A7}$$

and the Hamilton function is

$$H_i = -\mathcal{L}_i + \dot{\mathbf{q}}_i \cdot \mathbf{p}_i, \tag{A8}$$

where $\mathbf{q}_i = (x_i, \psi_i)$ and $\mathbf{p}_i = (\partial\mathcal{L}_i/\partial\dot{x}_i, \partial\mathcal{L}_i/\partial\dot{\psi}_i)$. Advanced variational calculus gives the condition that must be satisfied at points A, B, and C (Fig. 3):

$$[H_2\delta s_2 - \mathbf{p}_2 \cdot \delta\mathbf{q}_2]_B^C + [H_1\delta s_1 - \mathbf{p}_1 \cdot \delta\mathbf{q}_1]_A^B$$
$$+ [H_{Z1}\delta s_{Z1} - \mathbf{p}_{Z1} \cdot \delta\mathbf{q}_{Z1}]_D^A + [H_3\delta s_3 - \mathbf{p}_3 \cdot \delta\mathbf{q}_3]_C^A$$
$$+ [H_{Z3}\delta s_{Z3} - \mathbf{p}_{Z3} \cdot \delta\mathbf{q}_{Z3}]_F^C + [H_{Z2}\delta s_{Z2} - \mathbf{p}_{Z2} \cdot \delta\mathbf{q}_{Z2}]_E^B = 0.$$
$$\tag{A9}$$

The positions of points A, B, and C are varied along the three radial lines determined by ϕ_1, ϕ_2, and ϕ_3. In any of the three points $\delta\psi = 0$, whereas $\delta x_i = \delta s_i \cos\psi_i$. The variations of arclengths are not independent:

$$
\begin{aligned}
\delta s_{1B} &= -\delta s_{Z2B} = -\delta s_{2B}, \\
\delta s_{1A} &= \delta s_{Z1A} = -\delta s_{3A}, \\
\delta s_{3C} &= \delta s_{Z3C} = -\delta s_{2C}.
\end{aligned}
\tag{A10}
$$

Because points A, B, and C are independent of each other, the condition in Eq. (A9) at, e.g., point B can be rewritten as

$$
-H_{2B} + H_{Z2B} - H_{1B} = 0,
\tag{A11}
$$

which gives

$$
\dot{\psi}_{2B}^2 + \dot{\psi}_{1B}^2 = 4\gamma.
\tag{A12}
$$

Here $\dot{\psi}_{2B}$ and $\dot{\psi}_{1B}$ are the dimensionless curvatures of contour 2 and 1, respectively, at point B. A similar condition is obtained for points A and C. For a given set of angles ϕ_1, ϕ_2, and ϕ_3, the coordinates of points A, B, and C satisfy these constraints. In this way we obtain the energy and the shapes of the contours for arbitrary ϕ_1, ϕ_2, and $\phi_3 = 2\pi - \phi_1 - \phi_2$.

[1] D. W. Thompson, *On Growth and Form* (Cambridge University Press, Cambridge, 1917).

[2] H. Honda, M. Tanemura, and S. Imayama, J. Invest. Dermatol. **106**, 312 (1996).

[3] B. Dubertret and N. Rivier, Biophys. J. **73**, 38 (1997).

[4] M. C. Gibson, A. B. Patel, R. Nagpal, and N. Perrimon, Nature (London) **442**, 1038 (2006).

[5] S. F. Gilbert, *Developmental Biology* (Sinauer Associates, Sunderland, 2006).

[6] F. T. Lewis, Anat. Rec. **38**, 341 (1928).

[7] T. Hayashi and R. W. Carthew, Nature (London) **431**, 647 (2004).

[8] K. J. Dormer, *Fundamental Tissue Geometry for Biologists* (Cambridge University Press, Cambridge, 1980).

[9] D. N. Menton, J. Invest. Dermatol. **66**, 283 (1976).

[10] B. Alberts, A. Johnson, J. Lewis, M. Raff, T. Roberts, and P. Walter, *Essential Cell Biology* (NY Garland, New York, 2004).

[11] R. Farhadifar, J. C. Röper, B. Algouy, S. Eaton, and F. Jülicher, Curr. Biol. **17**, 2095 (2007).

[12] J. Käfer, T. Hayashi, A. F. M. Marée, R. W. Carthew, and F. Graner, Proc. Natl. Acad. Sci. USA **140**, 18549 (2007).

[13] S. Hilgenfeldt, S. Erisken, and R. W. Carthew, Proc. Natl. Acad. Sci. USA **105**, 907 (2008).

[14] M. L. Manning, R. A. Foty, M. S. Steinberg, and E.-M. Schoetz, Proc. Natl. Acad. Sci. USA **107**, 12517 (2010).

[15] E. A. Evans and D. A. Calderwood, Science **316**, 1148 (2007).

[16] B. Pfeuty and K. Kaneko, Phys. Biol. **4**, 194 (2007).

[17] M. S. Steinberg, Science **141**, 401 (1963).

[18] M. S. Steinberg, Curr. Opin. Genet. Dev. **17**, 281 (2007).

[19] D. J. Montell, Science **322**, 1502 (2008).

[20] A. C. Oates, N. Gorfinkiel, M. González-Gaitán, and C. P. Heisenberg, Nat. Rev. Genet. **10**, 517 (2009).

[21] U. Seifert, Adv. Phys. **46**, 13 (1997).

[22] J. Derganc, B. Božič, S. Svetina, and B. Žekš, Biophys. J. **84**, 1486 (2003).

[23] S. Svetina and P. Ziherl, Bioelectrochemistry **73**, 84 (2008).

[24] P. Ziherl, Phys. Rev. Lett. **99**, 128102 (2007).

[25] W. Helfrich, Z. Naturforsch. C **28**, 693 (1973).

[26] S. Svetina and B. Žekš, Eur. Biophys. J. **17**, 101 (1989).

[27] P. Ziherl and S. Svetina, Proc. Natl. Acad. Sci. USA **104**, 761 (2007).

[28] B. Božič, S. Svetina, B. Žekš, and R. E. Waugh, Biophys. J. **61**, 963 (1992).

[29] P. Ziherl and S. Svetina, Soft Matter **4**, 1937 (2008).

[30] U. Seifert and R. Lipowsky, Phys. Rev. A **42**, 4768 (1990).

[31] L. Fejes-Toth, *Regular Figures* (Macmillian, New York, 1964).

[32] F. Morgan, Proc. Am. Math. Soc. **122**, 1153 (1994).

[33] O. Aberth, J. London Math. Soc. **6**, 382 (1973).

[34] D. Weaire and R. Phelan, Philos. Mag. Lett. **69**, 107 (1994).

[35] Z. A. Melzak, Can. Math. J. **8**, 565 (1965).

[36] B. K. Vainshtein, *Fundamentals of Crystals* (Springer-Verlag, Berlin, 1994).

[37] M. Dubois, B. Deme, T. Gulik-Krzywicki, J. C. Dedieu, C. Vautrin, S. Desert, E. Perez, and T. Zemb, Nature (London) **411**, 672 (2001).

[38] M. Dubois, V. Lizunov, A. Meister, T. Gulik-Krzywicki, J. M. Verbavatz, E. Perez, J. Zimmerberg, and T. Zemb, Proc. Natl. Acad. Sci. USA **101**, 15082 (2004).

[39] C. A. Haselwandter and R. Phillips, Phys. Rev. Lett. **105**, 228101 (2010).

[40] T. D. Allen and C. S. Potten, Nature (London) **264**, 545 (1976).

[41] M. Rauzi, P. F. Lenne, and T. Lecuit, Nature (London) **468**, 1110 (2010).

[42] A. Hočevar and P. Ziherl, Phys. Rev. E **80**, 011904 (2009).

[43] T. F. Zhu and J. W. Szostak, PLoS ONE **4**, e5009 (2009).

[44] J. Derganc, S. Svetina, and B. Žekš, J. Theor. Biol. **260**, 333 (2009).

[45] R. Gabbrielli, Philos. Mag. Lett. **89**, 483 (2009).